processes

MDPI

Article

Analysis of Spatiotemporal Characteristics of Microseismic Monitoring Data in Deep Mining Based on ST-DBSCAN Clustering Algorithm

Jingxiao Yu [1,2,†], Hongsen He [1,†], Zongquan Liu [1], Xinzhe He [1], Fengwei Zhou [1], Zhihao Song [1] and Dingding Yang [1,2,*]

[1] School of Petrochemical Engineering and Environment, Zhejiang Ocean University, Zhoushan 316022, China; jingxiaoflyfish@zjou.edu.cn (J.Y.); 17369882829@163.com (H.H.); lzq2060953509@163.com (Z.L.); 18259983625@163.com (X.H.); zfw1155@163.com (F.Z.); szh19863765221@163.com (Z.S.)

[2] National & Local Joint Engineering Research Center of Harbor Oil & Gas Storage and Transportation Technology/Zhejiang Key Laboratory of Pollution Control for Port-Petrochemical Industry, Zhejiang Ocean University, Zhoushan 316022, China

* Correspondence: yangdd@zjou.edu.cn

† These authors contributed to the work equally and should be regarded as co-first authors.

Abstract

Analyzing the spatiotemporal characteristics of microseismic monitoring data is crucial for the monitoring and early prediction of coal–rock dynamic disasters during deep mining. Aiming to address the challenges hampering the early prediction of coal–rock dynamic disasters in deep mining, in this paper, we propose a method for analyzing the spatiotemporal characteristics of microseismic events in deep mining based on the ST-DBSCAN algorithm. First, a spatiotemporal distance metric model integrating temporal and spatial distances was constructed to accurately describe the correlations between microseismic events in spatiotemporal dimensions. Second, along with the spatiotemporal distribution characteristics of microseismic data, we determined the spatiotemporal neighborhood parameters suitable for deep-mining environments. Finally, we conducted clustering analysis of 14 sets of actual microseismic monitoring data from the Xinjulong Coal Mine. The results demonstrate the precise identification of two characteristic clusters, namely middle-layer mining disturbances and deep-seated activities, along with isolated high-magnitude events posing significant risks.

Keywords: deep mining; coal–rock dynamic disasters; spatiotemporal clustering; ST-DBSCAN; dynamic monitoring

check for updates

Academic Editors: Guanghui Zhao, Tingzhuang Han, Tao Meng, Gan Feng and Reza Taherdangkoo

Received: 29 May 2025
Revised: 15 July 2025
Accepted: 22 July 2025
Published: 24 July 2025

Citation: Yu, J.; He, H.; Liu, Z.; He, X.; Zhou, F.; Song, Z.; Yang, D. Analysis of Spatiotemporal Characteristics of Microseismic Monitoring Data in Deep Mining Based on ST-DBSCAN Clustering Algorithm. *Processes* **2025**, *13*, 2359. https://doi.org/10.3390/pr13082359

Copyright: © 2025 by the authors. Licensee MDPI, Basel, Switzerland. This article is an open access article distributed under the terms and conditions of the Creative Commons Attribution (CC BY) license (https://creativecommons.org/licenses/by/4.0/).

1. Introduction

As the world's largest coal-producing country, China produces approximately 40% of the total amount of coal worldwide, and it also consumes the most coal. The coal industry is a pillar of China's economy, accounting for about 60% of its total output and sales of primary energy. It has been projected that this proportion will be around 50% by 2050 [1–4]. Based on data compiled by the National Bureau of Statistics, China's coal consumption as a proportion of its total energy consumption over the past 10 years is shown in Figure 1. This figure indicates that coal will remain the dominant resource in China's energy structure for the foreseeable future. Currently, underground mining is the primary method used in over 95% of China's coal mines. Owing to complex geological conditions and frequent underground natural disasters such as gas outbursts, water inrushes, fires, and dust

accumulation, coal mine disasters remain difficult to control [5]. Among China's verified coal reserves, 19.97% are located at depths shallower than 1000 m, 21.08% can be found at depths of 1000–2000 m, and 58.95% exist at depths of 2000–4000 m. The average mining depth in China, including more than 210 coal mines operating at 800 m and over 60 ultra-deep mines exceeding 1000 m, is approaching 500 m. With the continued advancement of shallow resource extraction, the depth of coal mining is increasing at a rate of 10 to 25 m per year. The problems and hidden dangers in deep coal mining are far more complex than those in shallow mining. After entering the deep-mining stage, some coal mines will evolve from low-gas mines to high-gas and outburst-prone mines. Consequently, gas disasters will become increasingly severe, the risk of rock bursts will rise significantly, and new coal–rock dynamic disasters involving the coupling of coal and gas outbursts with rock bursts will occur. These factors will lead to overlapping risk factors in coal mining, making accidents such as gas outbursts, water inrushes, and rock bursts more frequent. The complexity of coal seam structures and geological conditions further exacerbates coal–rock dynamic disasters, threatening the safety of mining operations [6–8]. Therefore, in the coal industry, achieving effective monitoring and precise early prediction of coal–rock dynamic disasters in deep mining has become a critical challenge requiring urgent resolution.

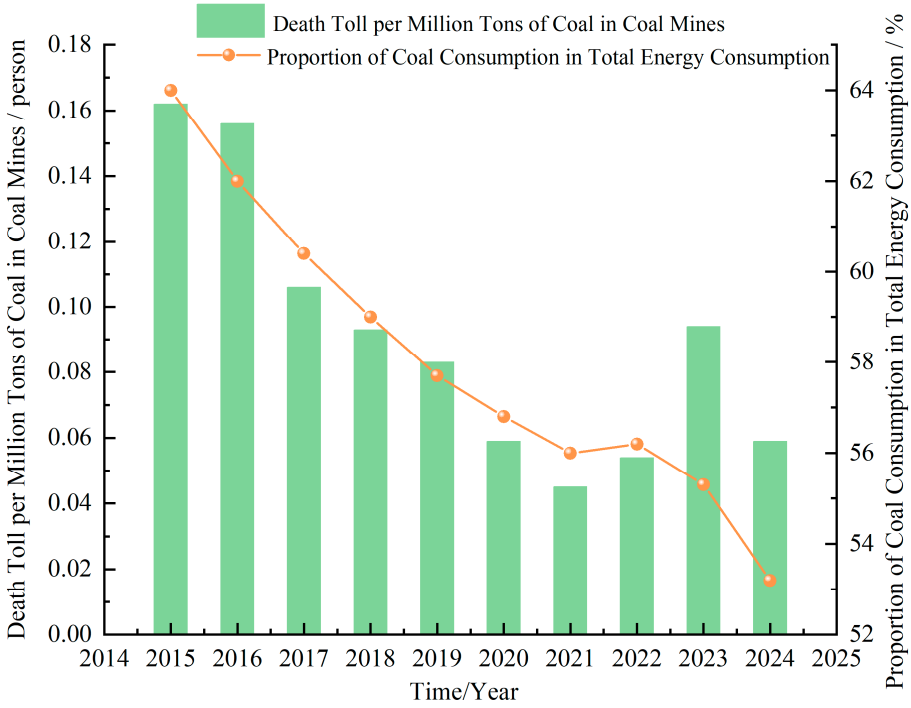


Figure 1. Data on China's coal consumption as a proportion of its total energy consumption over the past 10 years.

Microseismic events are significant precursors or triggers for dynamic disasters, but they are not disasters per se; they constitute a dynamic disaster only when they reach sufficient intensity to cause damage. Thanks to its high positioning accuracy, advanced automation, and reliable early-warning capabilities, microseismic monitoring technology has become indispensable in geotechnical engineering and mining, offering critical insights into underground activities and structural stability analysis [9,10]. As this technology continues to be adopted and refined, it is increasingly being recognized as a pivotal solution for managing complex coal–rock dynamic disasters in deep mines. Widely recognized by researchers in the coal-mining sector, it has progressively evolved into a core technology for addressing pressing challenges such as rock burst mitigation in deep shafts and gas outburst prevention in high-gas environments [11–15].

Focusing on the field of coal mining, Huang et al. [16] emphasized the applicability value of microseismic monitoring in relation to fully mechanized top-coal caving faces of extra-thick coal seams. Their research indicated that high-precision acquisition of microseismic data facilitates a deep understanding of surrounding rock movement behaviors and trends, thereby providing a basis for mining design and strata pressure control strategies. Similarly, Zhang et al. [17] highlighted the significance of microseismic monitoring in terms of coal mine safety, revealing its ability to monitor the failure mechanisms of coal–rock masses and energy transmission processes—critical for predicting and controlling disasters such as rock bursts. Cai et al. [18,19] utilized microseismic monitoring to analyze dynamic mine development, proposing a fuzzy comprehensive evaluation method for rock burst prediction. They also integrated strain energy transfer with coal burst mechanisms to develop the "Burst Strain Energy (BSE)" index. Shi et al. [20] established a rock mass stability monitoring system in deep mines, using microseismic technology to develop a monitoring network tailored to mine-specific conditions. By calibrating wave velocities through fixed-point blasting, they improved the accuracy of monitoring data.

The integration of microseismic data with advanced analytical technologies is equally remarkable. Dong et al. [21] introduced a Convolutional Neural Network (CNN) model to distinguish microseismic events induced by mining activities from those caused by blasting, demonstrating the potential of machine learning in seismic waveform analysis. This method enhances the accuracy of event classification, which is critical for operational safety and monitoring efficiency. Cao Anye et al. [22] conducted research on efficiently and accurately capturing and locating low-signal-to-noise-ratio seismic waves in mines, using millions of seismic wave data collected by traditional microseismic monitoring systems as samples. Yang et al. [23] proposed a spatiotemporal prediction method for rock bursts based on a Bidirectional Long Short-Term Memory Network (Bi-LSTM), improving the accuracy of rock burst disaster prediction. Song et al. [24] employed Bayesian inversion to analyze mining-induced vibrations in China's Xinzhuang Coal Mine, determining the types and parameters of source ruptures and exploring their relationships with rock bursts. This research provides a basis for analyzing and preventing similar vibrations.

Collectively, these studies demonstrate that the use of microseismic monitoring technology is a comprehensive, adaptable, and increasingly mature approach. Integrating multi-source data fusion with spatiotemporal analysis techniques offers new insights useful for the monitoring and early prediction of coal–rock dynamic disasters. In this study, we aimed to evaluate the clustering efficiency of ST-DBSCAN in identifying micro-seismic event patterns in deep coal mines, with an emphasis on early-warning capabilities. The ST-DBSCAN method was chosen because of its intrinsic ability to maintain spatiotemporal integrity, simultaneously processing spatial coordinates, depth, temporal sequences, and event magnitudes within a unified density framework, a feat that cannot be accomplished when using conventional spatial clustering methods (e.g., K-means). This research addresses two fundamental questions: Q1: How do depth-dependent geomechanical properties affect the spatiotemporal clustering characteristics of microseismic events? Q2: Can ST-DBSCAN outperform traditional methods in the early identification of high-risk isolated events ($M > 1.0$) under complex mining conditions? The existing studies mostly focus on the basic application of algorithms and lack in-depth analyses of the multi-dimensional correlations of microseismic events in terms of "energy–depth–spatiotemporal aspects", limiting the guiding value of clustering results for the early prediction of coal–rock dynamic disasters. In this study, we constructed a depth–magnitude coupled spatiotemporal distance model, designed a dynamic parameter determination method, and determined the correlations between clustering results and disaster mechanisms.

2. Materials and Methods

DBSCAN (Density-Based Spatial Clustering of Applications with Noise) is a density-based spatial clustering algorithm that is robust to noisy datasets (i.e., outliers or anomalies) [25,26]. ST-DBSCAN, an extension of DBSCAN that incorporates spatial and temporal dimensions, is a spatiotemporal density-clustering method used to identify correlations in data analyses of microseismic events in coal mines. As a density-based clustering algorithm, ST-DBSCAN can automatically recognize clusters of arbitrary shapes and treat outliers as noise. It defines density as the number of data points within a given radius, using this metric to classify data points into three categories: core points, border points, and noise points. By adopting spatiotemporal density as a similarity measure, ST-DBSCAN connects core object neighborhoods based on density thresholds to form irregular high-density connected clusters—maximal sets of density-connected points. Its advantages include its lack of a requirement to predefine the number of clusters, strong robustness, and ability to handle clusters of varying shapes, sizes, and densities. However, it may fail to cluster effectively when applied to datasets with uniformly distributed densities.

2.1. Related Concepts

ST-DBSCAN describes the compactness of a sample set based on a set of spatiotemporal neighborhoods. The concepts related to this algorithm are largely consistent with those for the DBSCAN algorithm, but the former does not require the number of clusters to be specified and can detect clusters of arbitrary shapes and sizes, demonstrating strong robustness to noise and outliers [27,28].

Core Definitions for the DBSCAN Algorithm

(1) ε-Neighborhood: For a sample point p, the point's ε-neighborhood is defined as the set of all sample points within a distance less than or equal to ε from p.
(2) Core Point: Within an ε-neighborhood (defined by a radius ε), if a sample point has at least MinPts (a minimum number of samples) within its ε-neighborhood, it is termed a core point.
(3) Border Point: A sample point p is a border point if the number of samples in its ε-neighborhood is less than MinPts but p lies within the ε-neighborhood of some core point.
(4) Noise Point: A noise point is a sample point that is neither a core point nor a border point.
(5) Directly Density-Reachable: If a point q lies within the ε-neighborhood of a core point p, then q is directly density-reachable from p.
(6) Density-Reachable: A point q is density-reachable from a point p if there exists a sample chain (p_1, p_2, . . ., p_n) where (p1 = p), p_n = q, and each p_{i+1} is directly density-reachable from pi.
(7) Density-Connected: Two points p and q are density-connected if there exists a core point o, such that both p and q are density-reachable from o.
(8) Cluster: A cluster is a maximal set of density-connected sample points satisfying the following conditions: any two points within the cluster are density-connected, and the cluster contains at least one core point.

Given above are the core definitions of the DBSCAN algorithm, and a description of its operating principle is given in Figure 2.

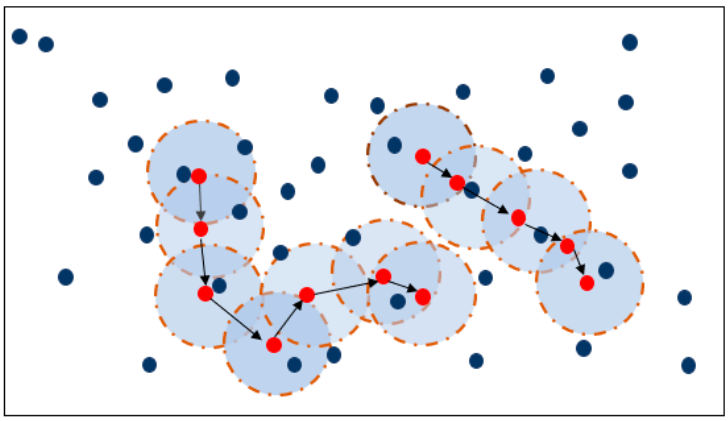


Figure 2. A schematic diagram of the DBSCAN algorithm.

The ST-DBSCAN algorithm extends DBSCAN by adding a temporal dimension, expanding the neighborhood to a spatiotemporal neighborhood, thereby enabling the identification and processing of clusters in spatiotemporal data. The spatiotemporal neighborhood of an object is defined by two parameters, namely a spatial radius Eps and a time window t, meaning ST-DBSCAN uses a spatiotemporal threshold (Eps, t) to measure whether two points are adjacent, as illustrated in Figure 3. Table 1 summarizes the differences between the ST-DBSCAN and DBSCAN algorithms.

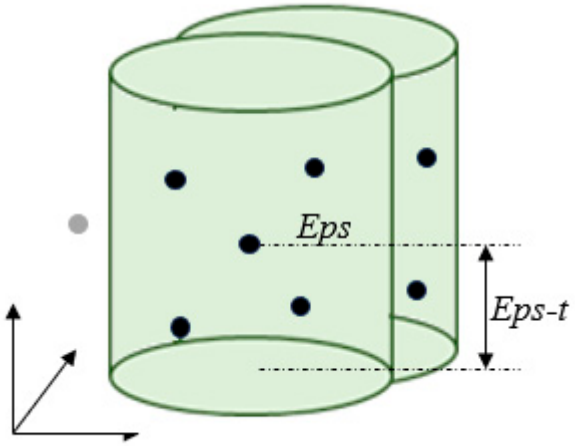


Figure 3. A schematic diagram of spatiotemporal neighborhoods.

Table 1. Differences between the ST-DBSCAN and DBSCAN algorithms.

Dimension	DBSCAN	ST—DBSCAN
Data Type	Purely spatial data (such as coordinate points)	Spatiotemporal data (space + timestamp)
Neighborhood Definition	Only spatial distance ε	Spatial distance εs + time difference εt
Cluster Characteristics	Spatial density-connected	Spatio-temporally density-connected (both space and time are adjacent)
Typical Applications	Spatial clustering (such as user location distribution)	Spatio-temporal pattern analysis (such as disaster event chains)

2.2. ST-DBSCAN Algorithm: Steps

A flowchart of the ST-DBSCAN clustering algorithm is shown in Figure 4; the algorithm involves the following key steps.

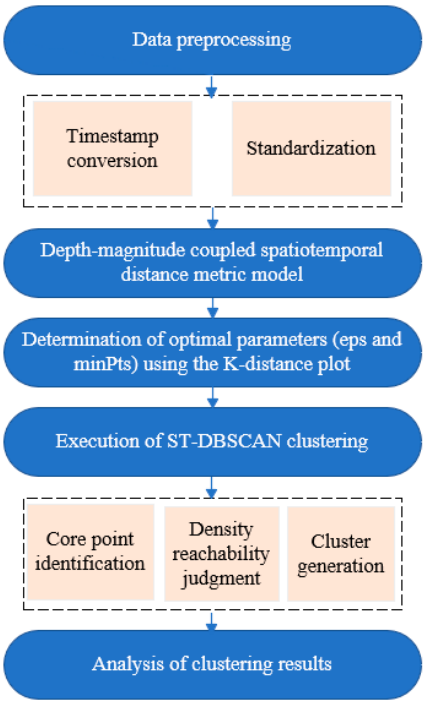


Figure 4. Flowchart of the ST-DBSCAN algorithm.

(1) Data Preprocessing

a. Time-Feature Engineering

Timestamp Conversion: Datetime values are converted into Unix timestamps (in seconds or milliseconds) for numerical computation.

b. Standardization

This process eliminates unit disparities, ensuring equitable weighting across dimensions (e.g., preventing temporal "seconds" from crowding out spatial "meters"). Raw data with different dimensions are transformed into standardized values (Z-score) to ensure equal weighting across dimensions:

$$X_{std} = \frac{X - \mu_X}{\sigma_X}, \quad (1)$$

$$Y_{std} = \frac{Y - \mu_Y}{\sigma_Y}, \quad (2)$$

$$Depth_{std} = \frac{Depth - \mu_{Depth}}{\sigma_{Depth}}, \quad (3)$$

$$t_{std} = \frac{t - \mu_t}{\sigma_t}, \quad (4)$$

where X and Y are the horizontal spatial coordinates of a microseismic event, D_{epth} is the vertical depth of the microseismic event, t is the timestamp of the microseismic event, μ_x is the mean value of X-coordinates, σ_x is the standard deviation of X-coordinates, X_{std} is the standardized X-coordinate, Ystd is the standardized Y-coordinate, σ_Y is the standard deviation of Y-coordinates, $Depth_{std}$ is the standardized depth, and t_{std} is the standardized timestamp.

After standardization, the data have a mean of 0 and a standard deviation of 1, so the influence of dimensional differences on distance calculation is avoided.

(2) Depth–Magnitude Coupled Weighted Spatiotemporal Distance

There is typically a significant correlation between mining depth and microseismic event magnitude [29], meaning that as mining depth increases, the magnitude (scale of energy release) of microseismic events tends to increase, justifying the addition of the magnitude term $w_m(M_i - M_j)^2$ to enhance clustering sensitivity to high-energy events. A magnitude weight can be incorporated into the distance formula:

$$d_{ST} = \sqrt{w_x(X_i - X_j)^2 + w_y(Y_i - Y_j)^2 + w_d(Depth_i - Depth_j)^2 + w_t(t_i - t_j)^2 + w_m(M_i - M_j)^2} \quad (5)$$

where w_x and w_y are the spatial weights for the X and Y dimensions, w_d is the weight for the depth dimension, M is the magnitude (energy-based) of a microseismic event, w_t is the weight for the temporal dimension, w_m is the weight for the magnitude dimension, and d_{ST} is the spatiotemporal-magnitude weighted distance.

The weighted Euclidean distance framework in Formula (5) incorporates three dimensions: spatial, temporal, and magnitude.

The spatial dimension integrates horizontal positions (X, Y) with vertical depth. Each weight is used to balance spatial anisotropy (e.g., deep-mining activities are more sensitive to vertical distances).

The temporal dimension enables isomorphic processing of temporal and spatial terms. Through standardization and the weight wt, spatiotemporal dimensions can be unified.

The magnitude dimension represents the difference in magnitude via a mathematical expression equivalent to spatiotemporal distance, allowing clustering to capture both spatiotemporal proximity and energy similarity simultaneously.

The allocation of each weight is determined based on actual cases to ensure balanced contribution of all dimensions.

The calculated spatiotemporal distance d_{ST} is iteratively compared to the threshold parameter ε during clustering. Specifically, if $d_{ST} \leq \varepsilon$, two points are considered adjacent in the spatiotemporal neighborhood. This threshold-based adjacency judgment is fundamental to density-connected cluster formation in ST-DBSCAN.

(3) ST-DBSCAN Parameter Setting

Based on the actual microseismic data, appropriate radius parameters (eps) and minimum sample parameters (minPts) are determined through experiments and cross-validation to ensure the accuracy and stability of the clustering results. This multi-parameter weighting strategy aligns with previous numerical modeling approaches used to simulate stress distribution and fracture evolution in cemented geomaterials [30].

By calculating the k-th nearest neighbor distance for each point, sorting these distances, and plotting the K-distance curve, the inflection point (knee point) can be set as eps, with minPts set to k + 1. Figure 5 provides information on ε determination.

(4) ST-DBSCAN Clustering Process

All data points are traversed, starting from core points, based on the spatial location information of microseismic events. Neighborhood points that meet the density criteria are recursively merged to form final clusters.

(5) Clustering Result Analysis

Different clusters are identified, including core mining activity zones and abnormal high-magnitude events, to characterize spatial–temporal patterns of microseismic activity.

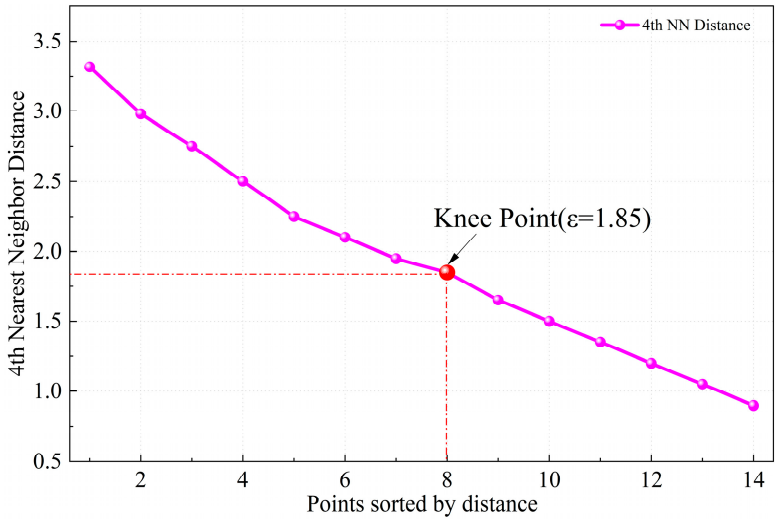


Figure 5. K-distance plot for ε determination.

2.3. Analysis Comparing ST-DBSCAN with Other Models

(1) ST-DBSCAN vs. OPTICS: ST-DBSCAN uses fixed spatiotemporal thresholds (Eps, t), while OPTICS generates a reachability plot to handle variable-density clusters.

(2) ST-DBSCAN vs. HDBSCAN: HDBSCAN automates cluster selection via hierarchy and density stability, reducing noise sensitivity. ST-DBSCAN relies on manual eps/minPts tuning (via K-distance plots).

ST-DBSCAN's features native spatiotemporal coupling (spatial distance + temporal window) critical for mining-disaster analysis (Table 1), while OPTICS and HDBSCAN lack built-in support for temporal dimensions.

3. Case Study

3.1. Event Background

Xinjulong Coal Mine is located in Longgu Town, Juye County, Heze City, Shandong Province. The mine field has a north–south strike length of 15 km, an east–west width of 12 km, and an area of approximately 180 km^2. The mine features complex geological structures. At the 2305S fully mechanized top-coal caving face, mining is carried out at seam No. 3, situated in the fifth working face of the south wing of the Second Mining Area at the −810 m level. The layout of the working face is shown in Figure 6. The coal seam strikes at 12–142°, dips at 102–232°, and has an average dip angle of 11°. The main faults include FD8, FD6, and FD11. Fault FD8 has a throw of 10–15 m and a dip angle of 70°. Fault FD6 has a throw of 0–10 m and a dip angle of 70°, while FD11 has a throw of 0–14 m and a dip angle of 70°.

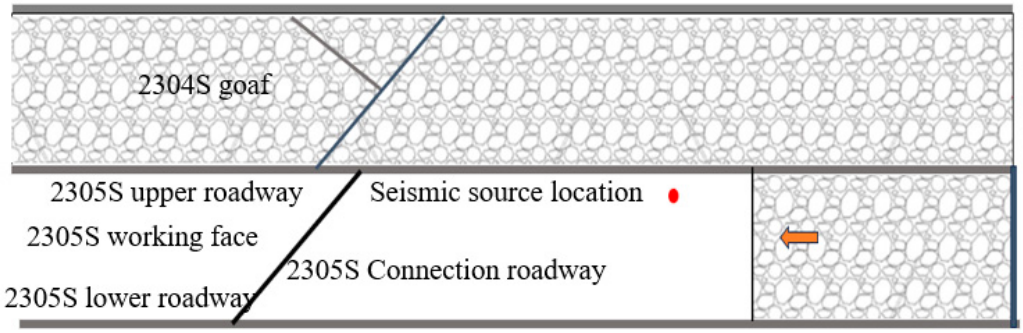


Figure 6. Planar layout of the working face.

An ARAMIS M/E microseismic monitoring system (comprising real-time monitoring recorders, analyzers, geophones, and a digital transmission system) was installed in the coal mine. As mining depth increased and the working face advanced toward the fault, the ARAMIS M/E system recorded 14 high-energy microseismic events (each > 10^4 J) in the 2305S working face from 22 February 2020 to 25 October 2021. Table 2 summarizes these 14 mining-induced microseismic events. The events occurred at depths ranging from 579 m to 1022 m (average depth: ~831 m), with frequent occurrences from March to October 2021 (12 out of 14 events), with a particular spike in July 2021 (5 events) [24].

Table 2. Coordinates and energy of microseismic events induced by deep mining [24].

No.	Date	X/m	Y/m	Depth/m	Energy/J	Location	Magnitude (Approximate)
1#	22 February 2020 6:17:22	20,399,987	3,911,232	790	4.25×10^7	2305S working face (960 m)	1.22
2#	28 February 2020 12:43:56	20,401,067	3,912,171	579	4.22×10^5	8303 working face (950 m)	0.55
3#	12 March 2021 16:33:09	20,399,938	3,910,924	908	2.57×10^5	2304 goaf (950 m)	0.47
4#	9 April 2021 22:49:52	20,400,440	3,911,937	1003	2.34×10^5	2306 lower roadway (1030 m)	0.44
5#	23 May 2021 13:25:01	20,399,242	3,911,958	816	6.12×10^4	Near 6304 goaf (860 m)	0.06
6#	21 June 2021 10:19:22	20,399,268	3,912,036	832	2.22×10^4	6304 goaf (840 m)	−0.23
7#	7 July 2021 0:20:34	20,398,797	3,913,277	792	1.69×10^4	6305 working face (800 m)	−0.38
8#	7 July 2021 22:10:43	20,399,149	3,912,091	827	1.68×10^4	6304 working face (840 m)	−0.38
9#	15 July 2021 10:54:07	20,401,335	3,910,800	1022	1.66×10^4	2308 working face (920 m)	−0.39
10#	22 July 2021 19:32:44	20,398,743	3,913,303	811	1.40×10^4	6304 lower roadway (790 m)	−0.49
11#	24 July 2021 12:11:22	20,401,475	3,909,804	906	1.34×10^4	2307 working face (860 m)	−0.48
12#	1 August 2021 14:17:22	20,401,184	3,912,266	953	1.30×10^4	8303 working face (970 m)	−0.45
13#	2 August 2021 9:32:49	20,399,603	3,911,483	845	1.14×10^4	Near 2303 working face (890 m)	−0.49
14#	25 October 2021 6:45:17	20,400,212	3,911,934	761	2.61×10^7	Near ventilation roadway of north district (990 m)	1.41

3.2. ST-DBSCAN Clustering Results

A three-dimensional (3D) visualization of the 14 microseismic events is depicted in Figure 7. The spatial coordinates and vertical depth of the events have the following ranges:

X-coordinates: These span from 20,398,743 m to 20,401,475 m (covering a horizontal distance of approximately 2732 m).

Y-coordinates: These range from 3,909,804 m to 3,913,277 m (a horizontal span of approximately 3473 m).

Vertical depth: This depth extends from 579 m to 1003 m (a vertical range of approximately 424 m).

Using the raw data from Table 2, we first converted the date and time information into Unix timestamps; the results are shown in Table 3. The microseismic events involve multiple parameters—X, Y, depth, time, and magnitude—with significant variations in units and scales across these dimensions, necessitating data standardization. The Z-score normalization method was applied, and the standardized results are presented in Tables 4 and 5.

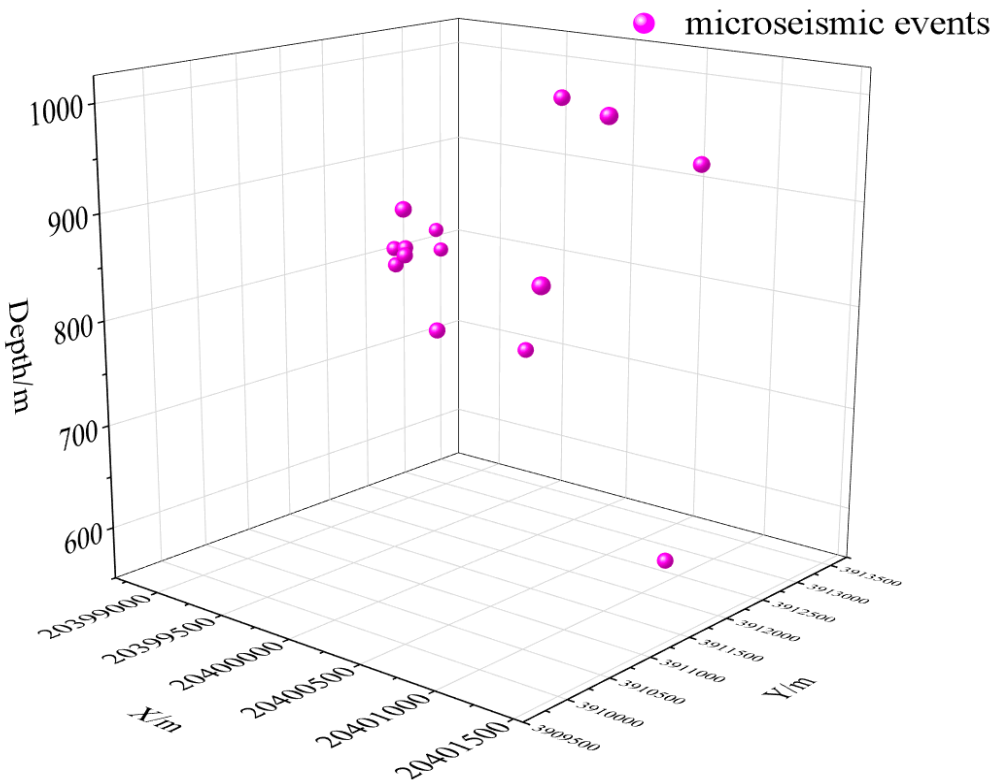


Figure 7. A three-dimensional spatial plot of microseismic events.

Table 3. Conversion of dates and times into timestamps.

No.	Time	Unix Timestamp (Seconds)	No.	Time	Unix Timestamp (Seconds)
1#	22 February 2020 6:17:22	1,582,347,442	8#	7 July 2021 22:10:43	1,625,688,243
2#	28 February 2020 12:43:56	1,582,903,436	9#	15 July 2021 10:54:07	1,626,341,647
3#	12 March 2021 16:33:09	1,615,566,789	10#	22 July 2021 19:32:44	1,626,982,364
4#	9 April 2021 22:49:52	1,618,003,792	11#	24 July 2021 12:11:22	1,626,908,482
5#	23 May 2021 13:25:01	1,621,776,301	12#	1 August 2021 14:17:22	1,627,817,842
6#	21 June 2021 10:19:22	1,624,275,562	13#	2 August 2021 9:32:49	1,627,904,569
7#	7 July 2021 0:20:34	1,625,607,634	14#	25 October 2021 6:45:17	1,635,125,117

Table 4. Means and standard deviations of each column's data.

Column Name(s)	Mean	Std
X/m	20,400,038.50	994.34
Y/m	3,911,746.50	885.56
Depth/m	858.00	130.38
Energy/J	3.34×10^6 (3,340,000)	1.13×10^7 (11,300,000)
Magnitude	−0.03	0.69
Unix (seconds)	1,620,409,330.21	19,485,439.34

Based on considerations of spatial dominance, the importance of depth, the balance between time and magnitude, and other aspects, the weights for each parameter were set as follows: spatial coordinates (X/Y), 0.25 each (total 0.5); depth, 0.2; time, 0.15; and magnitude, 0.15. All the weights sum to a total weight of 1.0. Using the Euclidean distance formula mentioned previously and K-distance plot analysis, we determined the spatial radius, temporal radius, and minimum sample size. The final clustering results are presented in Table 6. Events classified as noise points (#1, #11, #13, and #14) were excluded from clusters because of significant deviations in spatiotemporal or energy characteristics. ST-DBSCAN treats points as noise if they lack density-reachable neighbors within the

spatiotemporal-magnitude threshold (Section 2.1). These outliers fell outside the Eps-t energy bounds of the core clusters.

Table 5. Standardized data.

No.	X Scaled/m	Y Scaled/m	Depth Scaled/m	Energy Scaled/J	Magnitude Scaled	Unix Scaled/s
1#	1.96	−0.74	−0.52	3.46	1.81	−1.95
2#	1.04	0.05	−2.14	0.03	0.84	−1.92
3#	2.06	−0.93	0.39	−0.07	0.72	−0.23
4#	0.40	0.02	1.11	−0.09	0.67	0.09
5#	−0.84	0.02	−0.32	−0.24	0.04	0.59
6#	−0.81	0.08	−0.20	−0.27	−0.25	1.23
7#	−1.25	1.75	−0.50	−0.28	−0.51	1.80
8#	−0.90	0.16	−0.24	−0.28	−0.51	1.85
9#	1.30	−1.09	1.26	−0.28	−0.52	1.95
10#	−1.31	1.79	−0.36	−0.28	−0.67	2.08
11#	1.44	−2.12	0.37	−0.29	−0.65	2.04
12#	1.09	0.09	0.73	−0.29	−0.61	2.13
13#	−0.45	−0.37	−0.10	−0.28	−0.67	2.14
14#	0.17	0.02	−0.75	2.01	2.09	5.90

Table 6. Calculation results obtained using the ST-DBSCAN clustering algorithm.

No.	X/m	Y/m	Depth/m	Magnitude	Cluster	Spatiotemporal Characteristic Analysis
#1	20,399,987	3,911,232	790	1.22	−1	High magnitude, spatiotemporal isolation (edge region)
#2	20,401,067	3,912,171	579	0.55	2	Core cluster, shallow low-energy disturbance
#3	20,399,938	3,910,924	908	0.47	2	Core cluster, deep-mining activities
#4	20,400,440	3,911,937	1003	0.44	2	Core cluster, deep-mining activities
#5	20,399,242	3,911,958	816	0.06	1	Core cluster, middle-layer mining disturbance
#6	20,399,268	3,912,036	832	−0.23	1	Core cluster, middle-layer mining disturbance
#7	20,398,797	3,913,277	792	−0.38	1	Core cluster, middle-layer mining disturbance
#8	20,399,149	3,912,091	827	−0.38	1	Core cluster, middle-layer mining disturbance
#9	20,401,335	3,910,800	1022	−0.39	2	Core cluster, deep-mining activities
#10	20,398,743	3,913,303	811	−0.49	1	Core cluster, middle-layer mining disturbance
#11	20,401,475	3,909,804	906	−0.48	−1	Core cluster, middle-layer mining disturbance
#12	20,401,184	3,912,266	953	−0.45	2	Core cluster, deep-mining activities
#13	20,399,603	3,911,483	845	−0.49	−1	Core cluster, middle-layer mining disturbance
#14	20,400,212	3,911,934	761	1.41	−1	High magnitude, spatiotemporal isolation (edge region)

Further analysis of the temporal distribution characteristics of the clustering results based on Tables 3 and 6 shows that the five events in Cluster 1 occurred intensively from 23 May to 22 July 2021, with a time span of only 2 months, presenting a "dense outbreak" feature, which reflects the short-term aggregation effect of microseismic activities in shallow-middle mining. The five events in Cluster 2 occurred over a relatively large time span (from February 2020 to August 2021) with intervals of 3–18 months, showing a "long-term continuous" feature, which embodies the temporal lag of microseismic activities in deep, high-stress environments. Among the noise points, Event #1 and Event #14 are 20 months apart, both occurring near the fault zone, and the frequency of the preceding Cluster 2 events increased, suggesting that high-magnitude isolated events may be related to sudden release after long-term stress accumulation at great depths, providing key clues for disaster early warning in regard to the temporal dimension.

A clustering visualization is shown in Figure 8, displaying the clusters from three planar perspectives (horizontal, dip, and strike) and three-dimensionally. As shown in Figure 6, Cluster 1 (blue) reflects routine stress release in mid-layer mining zones (e.g., Faces 6304/6305), while Cluster 2 (red) correlates with deep-seated rock fracturing. Noise points (gray) exhibit outlier traits in space, time, or energy, indicating critical risks.

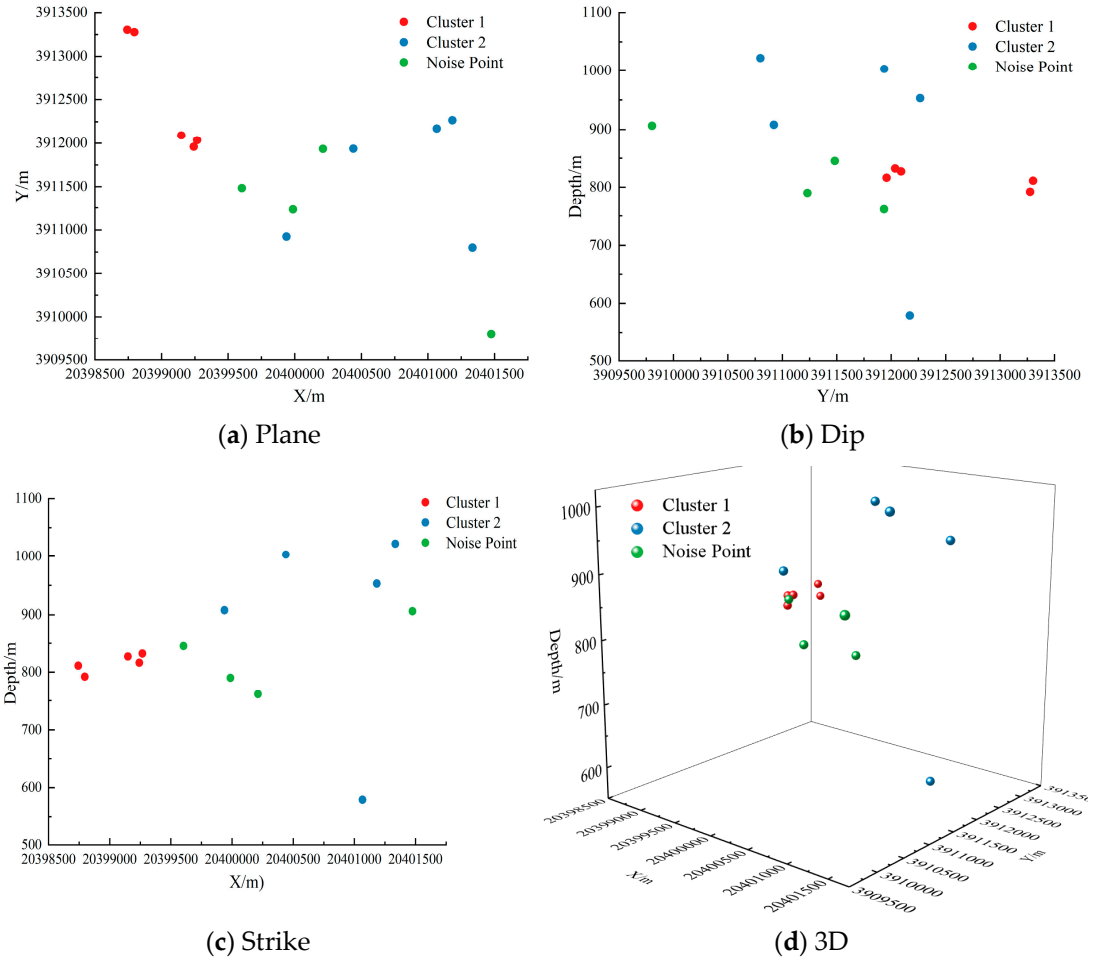


Figure 8. Spatiotemporal density clustering of microseismic events: (**a**) horizontal plane, (**b**) dip section, (**c**) strike section, and (**d**) 3D view.

In summary, magnitude and depth exhibit a strong coupling effect over mining cycles: Middle-layer mining disturbances primarily trigger low-magnitude, short-period clustered events; the deep high-stress environment fosters medium-to-high magnitude, long-period continuous activity, which, under specific geological and mining disturbance conditions, can culminate in isolated high-magnitude disaster events. This association between depth, magnitude, and temporal patterns provides crucial insights into the evolving mechanical behavior of coal-rock masses and disaster incubation mechanisms under deep mining conditions, significantly enhancing the early warning capability for disasters based on microseismic monitoring.

3.3. Design of the Comparative Experiment

In this study, DBSCAN and K-means, which are widely used in microseismic data analysis, were selected as benchmark algorithms [21,25] for comparison with the ST-DBSCAN algorithm in terms of its spatiotemporal fusion advantages. The comparison was mainly carried out according to three aspects: Silhouette Score, Davies–Bouldin Index (DB Index), and noise-point recognition rate. The results of the comparative experiment are shown in Table 7. ST-DBSCAN is significantly superior to the other two methods in terms of Silhouette Score, Davies–Bouldin Index (DB Index), and noise recognition rate, proving the effectiveness of spatiotemporal fusion in capturing microseismic patterns in deep mines.

Table 7. Results of the comparison.

Algorithm	Silhouette	DB Index	Noise Detection	Interpretability
ST-DBSCAN	0.62	0.81	100% (4/4)	Provides clear core/abnormal separation
DBSCAN	0.41	1.32	50% (2/4)	Ignores time and merges async events
K-means	0.38	1.45	25% (1/4)	Fails to detect noise (fixed k = 3)
OPTICS	0.55	0.95	75% (3/4)	Is sensitive to time windows and allows complex parameter tuning

4. Discussion

(1) **Calculations:**

Cluster 1 includes Events 5, 6, 7, 8, and 10, characterized by spatiotemporal proximity: these events are concentrated in May–July 2021 and occurred within the vicinity of the 6304/6305 working faces (with X/Y differences < 500 m). The magnitude ranges from −0.49 to 0.06, with low energy (1.40×10^4–6.12×10^4 J). Combined with mining progress, during this period, the 6304 working face was in the final stage of being mined, while the 6305 working face had just begun being mined. The propagation of surrounding rock fractures induced by mining disturbances was mainly gradual, and the microseismic activities exhibited "short cycle, low energy, and clustering" characteristics, reflecting the stable failure mode of shallow-middle rock masses under conventional mining conditions.

Cluster 2, a typical cluster of deep microseismic activities encompassing Events 2, 3, 4, 9, and 12, shows a strong spatial correlation with deep-mining disturbance zones: all events are concentrated in the mining areas of deep working faces (e.g., 2305S and 2306) at depths exceeding 900 m (constituting a high-stress environment). With magnitudes stably ranging from 0.44 to 0.55 and energy levels at a medium range of 1.30×10^4–4.22×10^5 J, this cluster spans 2020–2021 and exhibits distinct "long-cycle, medium-energy, and continuous" characteristics through the coupling of concentrated spatial coordinates and magnitude weights. Similar to cyclic thermal loading in backfill materials influencing subsurface energy accumulation [31–33], microseismic energy distribution in deep rock masses may also be shaped by repeated mechanical stress and localized heat buildup. This activity pattern is directly linked to the mechanical behavior of deep rock masses under high confining pressure: as mining depth increases, the elastic energy storage capacity of rock masses enhances, leading to slow accumulation and continuous release of microseismic energy—a typical response to deep fault activation and rock burst incubation. Its spatiotemporal distribution thus provides critical insights for analyzing precursor signals of dynamic disasters induced by deep mining.

The above clustering results reveal the intrinsic correlations between microseismic events with different spatiotemporal distributions and mining activities/geological environments. However, as a key factor affecting the stress states of deep rock masses and microseismic energy release, determining whether changes in depth will alter this correlation pattern requires further verification. Therefore, by fixing other parameters (spatiotemporal weights, magnitude weights, etc.) and only adjusting the depth parameter (±200 m, −400 m, +600 m, and +1000 m) for gradient simulation, the sensitivity of the clustering structure of microseismic events to depth can be explored.

(2) **Mining Depth Sensitivity Analysis:**

With the other parameters kept constant, depth gradient experiments were conducted by simulating different depths. Five adjustments were made: ±200 m, −400 m, +600 m, and +1000 m. The integration of deep learning for classification, as seen in subsurface corrosion detection [34], further validates the potential of intelligent algorithms in geomechanical risk analysis. The clustering results are shown in Table 8 and Figure 9. When depth was increased while the weights remained unchanged, the clustering structure re-

mained largely stable, but the number of noise points and high-energy abnormal events increased. Notably, this did not alter the inherent essence of the spatiotemporal correlation for microseismic events.

Table 8. Clustering results after depth adjustments.

Depth Adjustment	Cluster	Noise Point
Original(0)	[5, 6, 7, 8, 10], [2, 3, 4, 9, 12]	[1, 11, 13, 14]
−400	[5, 6, 7, 8, 10], [2, 3, 4, 9, 11, 12]	[1, 13, 14]
−200	[5, 6, 7, 8, 10], [2, 3, 4, 9, 12]	[1, 11, 13, 14]
+200	[5, 6, 8, 10], [2, 3, 4, 9, 12]	[1, 7, 11, 13, 14]
+600	[5, 6, 8, 10], [2, 3, 4, 9, 12]	[1, 7, 11, 13, 14]
+1000	[5, 6, 8, 10], [2, 3, 4, 9, 12]	[1, 7, 11, 13, 14]

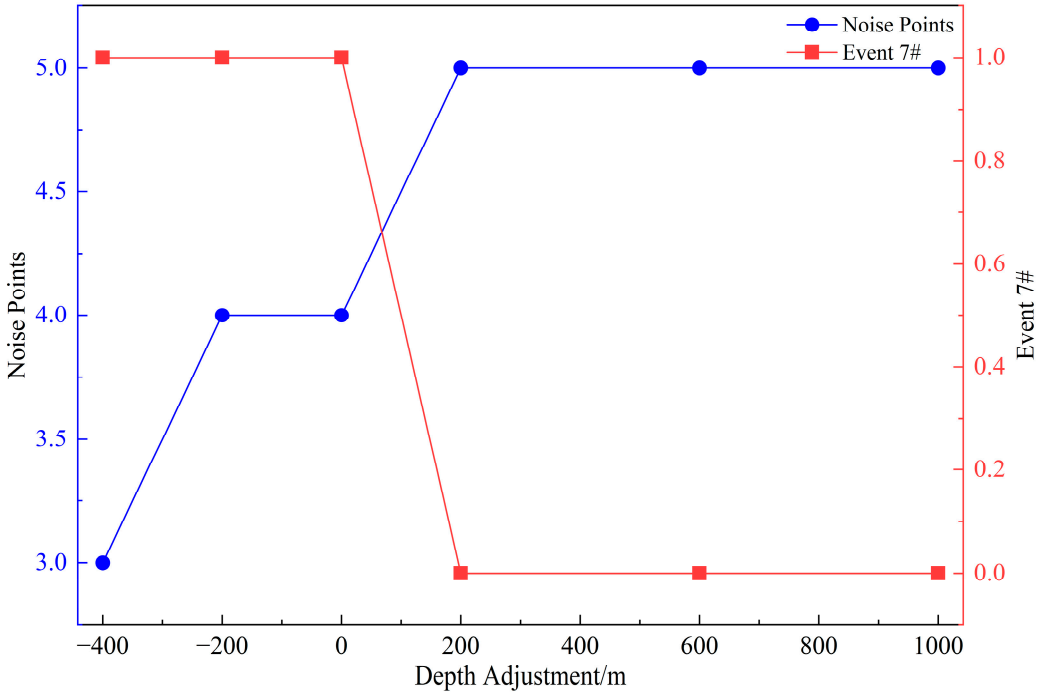


Figure 9. The impact of depth adjustments on the clustering results.

(3) **Comparison with Actual Disaster Data**

The noise points include Events 1 and 14, which are high-magnitude isolated events posing a risk of coal–rock dynamic disasters. Events 11 and 13 exhibit spatiotemporal or magnitude differences exceeding the threshold.

Event #1 was a coal–rock–gas composite dynamic disaster accident that occurred at 06:17:22 on 22 February 2020, in the upper entry of the 2305S fully mechanized top-coal caving face. As the working face advanced toward the fault, elastic strain energy accumulated in the fault zone, and the coal–rock mass was suddenly released, triggering impact instability in the coal–rock mass. The seismic source was located 90 m ahead of the 2305S working face, 31.2 m inside the solid coal side of the 2305S upper entry, and 160 m above the roof. The 2305S working face has a burial depth of approximately 1000 m, resulting in significantly increased in situ rock stress due to this great depth. The working face is situated in a wedge-shaped graben area formed by the FD8 and FD6 faults. Mining-induced disturbances triggered a fault slip, releasing strong seismic events in the mine that ultimately led to the mine disaster. Event #1 was identified as a noise point (Table 6), and its spatiotemporal isolation highly aligns with the actual accident (Event #1 was a coal–rock–gas compound dynamic disaster). These results demonstrate that ST-DBSCAN

can situate unconventional energy release events, which often indicate fault slippage or rock burst risks in deep mining.

5. Conclusions

(1) The core innovation of our ST-DBSCAN-based spatiotemporal analysis method for deep-mining microseismic data lies in its novel spatiotemporal clustering framework. This framework explicitly integrates both the temporal occurrence and spatial location attributes of microseismic events into a unified distance metric, effectively addressing the inherent limitations of traditional clustering algorithms (like DBSCAN), which typically handle spatial and temporal dimensions separately or inadequately. This integration directly leads to a significant enhancement in accurately identifying the complex spatiotemporal distribution patterns inherent in microseismic sequences.

(2) Key to this method's precision is the development of a tailored spatiotemporal distance metric model and the systematic optimization of spatiotemporal neighborhood parameters (Eps1 for space, and Eps2 for time), enabling the algorithm to discriminate and isolate distinct microseismic event clusters exhibiting diverse spatiotemporal characteristics (e.g., rapid bursts vs. prolonged swarms). Consequently, this method robustly delineates critical patterns such as temporal periodicity (e.g., shifts correlating with mining cycles or blasting schedules), spatial agglomeration zones (highlighting high-risk rock mass areas), and the dynamic spatiotemporal evolution and interaction pathways between these clusters over the monitoring period.

(3) The analysis results in relation to actual deep-mining microseismic monitoring data show that different microseismic event clusters correspond to different rock mass failure processes and mining activity impacts, providing an important basis for comprehensively understanding the mechanical behavior of rock masses and disaster incubation mechanisms during deep mining.

(4) To effectively monitor microseismic activities in longwall mining panels, we recommend adopting the following sensor layout strategy: "3D stereoscopic + key area densification". In addition, the sensor layout should be dynamically adjusted in line with mining progress so as to realize real-time tracking of microseismic activities and early prediction of disasters, ensuring safe and efficient operations in longwall mining.

Author Contributions: J.Y.: conceptualization, methodology, software, and writing—original draft; H.H.: writing—original draft and validation; Z.L.: methodology and validation; X.H.: visualization; F.Z.: conceptualization; Z.S.: visualization; D.Y.: supervision and visualization. All authors have read and agreed to the published version of the manuscript.

Funding: This work was supported by the Fundamental Research Funds for Zhejiang Provincial Universities and Research Institutes (JX6311021523). The authors are grateful for the funding provided by the 2024 National College Student Innovation and Entrepreneurship Training Program in Zhejiang Ocean University (202410340055).

Data Availability Statement: The original contributions presented in this study are included in the article. Further inquiries can be directed to the corresponding author.

Conflicts of Interest: The authors declare no conflicts of interest.

References

1. Wang, S.; Liu, L.; Zhu, M.; Shen, Y.; Shi, Q.; Sun, Q.; Fang, Z.; Ruan, S.; He, W.; Yang, P.; et al. New way for green and low-carbon development of coal under the target of "double carbon". *J. China Coal Soc.* **2024**, *49*, 152–171. [CrossRef]
2. Yu, J.; Li, Z.; Yang, D.; Liu, Y.; Fang, S. Experimental study on dynamic evolutions of airflow in the ventilation network under the effect of mine gas outburst disasters. *Sci. Rep.* **2025**, *15*, 10651. [CrossRef] [PubMed]

3. Yu, J.; Li, Z.; Yang, D.; Liu, Y. Dynamic Risk Assessment of Gas Accumulation During Coal and Gas Outburst Catastrophes Based on Analytic Hierarchy Process and Information Entropy. *Processes* **2025**, *13*, 1305. [CrossRef]
4. Yuan, L.; Wang, E.Y.; Ma, Y.K.; Liu, Y.; Li, X. Research progress of coal and rock dynamic disasters and scientific and technological problems in China. *J. China Coal Soc.* **2023**, *48*, 1825–1845. [CrossRef]
5. Yang, K.; Guo, P.H.; Yuan, L.; Cao, A.Y.; Zhang, Y.J.; Ma, Y.K.; Li, J.Z. Research progress on the conditions and mechanisms of typical dynamic disasters formation in deep coal mining. *J. China Coal Soc.* **2024**, *50*, 3352–3373. [CrossRef]
6. Zhang, G.R.; Wang, E.Y.; Zhang, C.L.; Li, Z.H.; Wang, D.M. A Comprehensive Risk Assessment Method for Coal and Gas Outburst in Underground Coal Mines Based on Variable Weight Theory and Uncertainty Analysis. *Process Saf. Environ. Prot.* **2022**, *167*, 97–111. [CrossRef]
7. Zhang, G.R.; Wang, E.; Liu, X.; Li, Z. Research on Risk Assessment of Coal and Gas Outburst During Continuous Excavation Cycle of Coal Mine with Dynamic Probabilistic Inference. *Process Saf. Environ. Prot.* **2024**, *190*, 405–419. [CrossRef]
8. Fang, S.; Yin, S.; Li, Z.; Yang, D.; Wang, D.; Ding, Z.; Li, G. Study on the adsorption characteristics and pore-fissure response mechanism of meagre coal and anthracite under different methane pressures. *Energy* **2025**, *332*, 137283. [CrossRef]
9. Cheng, J.; Song, G.; Sun, X.; Wen, L.; Li, F. Research developments and prospects on microseismic source location in mines. *Engineering* **2018**, *4*, 653–660. [CrossRef]
10. Kinscher, J.; Bernard, P.; Contrucci, I.; Mangeney, A.; Piguet, J.P.; Bigarre, P. Location of microseismic swarms induced by salt solution mining. *Geophys. J. Int.* **2015**, *200*, 337–362. [CrossRef]
11. Dou, L.M.; Cao, J.R.; Cao, A.Y.; Chai, Y.J.; Bai, J.Z.; Kan, J.L. Study on the types of coal mine seismicity and the propagation law of seismic waves. *Coal Sci. Technol.* **2021**, *49*, 23–31. [CrossRef]
12. Zhu, G.A.; Jiang, Q.P.; Wu, Y.P.; Dou, L.M.; Lin, Z.Q.; Liu, H.Y. Numerical inversion of fault slip instability under stress wave disturbance. *J. Min. Saf. Eng.* **2021**, *38*, 370–379. [CrossRef]
13. Song, D.Z.; He, X.Q.; Dou, L.M.; Zu, Z.Y.; Wang, A.H.; Li, Z.L. Research on detection technology of microseismic area with coal seam outburst risk. *China Saf. Sci. J.* **2021**, *31*, 89–94. [CrossRef]
14. Cai, W.; Dou, L.M.; Wang, G.F.; Hu, Y.W. Mechanical mechanism of fault activation caused by coal seam mining activities and its induced rockburst mechanism. *J. Min. Saf. Eng.* **2019**, *36*, 1193–1202. [CrossRef]
15. Zhu, G.A.; Jiang, Q.P.; Wu, Y.P.; Dou, L.M.; Xie, J.H.; Wang, C.; Liu, H.Y. Determination of reasonable final mining line position in deep working face based on "stress field-seismic wave field". *J. China Coal Soc.* **2020**, *45* (Suppl. S2), 571–580. [CrossRef]
16. Huang, Q.G.; Gao, F. Application of Microseismic Monitoring Technology on Fully Mechanized Top-coal Caving Face of Extra-thick Coal Seam. In Proceedings of the 2011 International Conference on Multimedia Technology, Hangzhou, China, 26–28 July 2011. [CrossRef]
17. Zhang, C.; Jin, G.H.; Liu, C.; Li, S.G.; Xue, J.H.; Cheng, R.H.; Wang, X.L.; Zeng, X.Z. Prediction of Rockbursts in A Typical Island Working Face of A Coal Mine Through Microseismic Monitoring Technology. *Tunn. Undergr. Space Technol.* **2021**, *110*, 103827. [CrossRef]
18. Cai, W.; Dou, L.M.; Zhang, M.; Chen, W.Z.; Shi, J.Q.; Fan, L.F. A Fuzzy Comprehensive Evaluation Methodology for Rock Burst Forecasting Using Microseismic Monitoring. *Tunn. Undergr. Space Technol.* **2018**, *80*, 232–245. [CrossRef]
19. Cai, W.; Dou, L.M.; Si, G.Y.; Cao, A.Y.; Gong, S.Y.; Wang, G.F.; Yuan, S.S. A New Seismic-Based Strain Energy Methodology for Coal Burst Forecasting in Underground Coal Mines. *Int. J. Rock Mech. Min. Sci.* **2019**, *123*, 104086. [CrossRef]
20. Shi, F.; Zhang, D.; Wang, P.; Cai, Y.; Yuan, B. Investigation on Rock Mass Stability Monitoring System and Activity Characteristic in Deep Mining. *MATEC Web Conf.* **2022**, *356*, 01009. [CrossRef]
21. Dong, L.J.; Tang, Z.; Li, X.B.; Chen, Y.C.; Xue, J.C. Discrimination of mining microseismic events and blasts using convolutional neural networks and original waveform. *J. Cent. South Univ. Technol.* **2020**, *27*, 3078–3089. [CrossRef]
22. Cao, A.Y.; Yang, X.; Wang, C.B.; Li, S.; Liu, Y.Q. High-precision phase picking and automatic source locating method for seismicity in mines based on deep transfer learning. *J. China Coal Soc.* **2023**, *48*, 4393–4405. [CrossRef]
23. Yang, X.; Li, Y.P.; Cao, A.Y.; Li, Y.Q.; Wang, C.B.; Zhang, W.W.; Niu, Q. Coal Burst Spatio-Temporal Prediction Method Based on Bidirectional Long Short-Term Memory Network. *Int. J. Coal Sci. Technol.* **2025**, *12*, 11. [CrossRef]
24. Song, J.F.; Li, C.P.; Zhang, X.F.; Sun, C.H.; Zhang, J.; Zhang, Z.G. Application of Bayesian Method for Mining-Induced Tremors: A Case Study of the Xinjulong Coal Mine in China. *Int. J. Rock Mech. Min. Sci.* **2024**, *174*, 105642. [CrossRef]
25. Ester, M.; Kriegel, H.P.; Sander, J.; Xu, X. A density-based algorithm for discovering clusters in large spatial databases with noise. In Proceedings of the 2nd International Conference on Knowledge Discovery and Data Mining (KDD'96), Portland, OR, USA, 2–4 August 1996; pp. 226–231. [CrossRef]
26. Zhang, X.; Chen, Y.; Jia, J.; Kuang, K.; Lan, Y.; Wu, C. Multi-view density-based field-road classification for agricultural machinery: DBSCAN and object detection. *Comput. Electron. Agric.* **2022**, *200*, 107263. [CrossRef]
27. Zhang, G.H. Analysis of spatio-temporal characteristics of mine rock burst microseismic monitoring data based on ST-DBSCAN clustering algorithm. *China Energy Environ. Prot.* **2024**, *46*, 62–70. [CrossRef]

28. Li, Y. Research on Vessel Behavior Recognition Method Based on Spatial-Temporal Movement Features. Master's Thesis, Dalian Maritime University, Dalian, China, 2024.
29. Rong, H.; Wei, S.L.; Zhang, H.W.; Chen, L.; Li, N. Influencing factors and distribution characteristics of rock burst under complex geological dynamic environment. *Coal Sci. Technol.* **2025**, *53*, 423–434.
30. Rizvi, Z.H.; Mustafa, S.H.; Sattari, A.S.; Ahmad, S.; Furtner, P.; Wuttke, F. Dynamic Lattice Element Modelling of Cemented Geomaterials. In *Advances in Computer Methods and Geomechanics*; Prashant, A., Sachan, A., Desai, C., Eds.; Lecture Notes in Civil Engineering; Springer: Singapore, 2020; Volume 55, pp. 689–701. [CrossRef]
31. Ahmad, S.; Ahmad, S.; Akhtar, S.; Rizvi, Z.H.; Wuttke, F. Data-driven assessment of corrosion in reinforced concrete structures embedded in clay dominated soils. *Sci. Rep.* **2025**, *15*, 22744. [CrossRef] [PubMed]
32. Ahmad, S.; Rizvi, Z.H.; Arp, J.C.C.; Wuttke, F.; Tirth, V.; Islam, S. Evolution of Temperature Field around Underground Power Cable for Static and Cyclic Heating. *Energies* **2021**, *14*, 8191. [CrossRef]
33. Ahmad, S.; Rizvi, Z.H.; Wuttke, F. Unveiling soil thermal behavior under ultra-high voltage power cable operations. *Sci. Rep.* **2025**, *15*, 7315. [CrossRef] [PubMed]
34. Ahmad, S.; Rizvi, Z.H.; Khan, M.A.; Ahmad, J.; Wuttke, F. Experimental study of thermal performance of the backfill material around underground power cable under steady and cyclic thermal loading. *Mater. Today Proc.* **2019**, *17*, 85–95. [CrossRef]

Disclaimer/Publisher's Note: The statements, opinions and data contained in all publications are solely those of the individual author(s) and contributor(s) and not of MDPI and/or the editor(s). MDPI and/or the editor(s) disclaim responsibility for any injury to people or property resulting from any ideas, methods, instructions or products referred to in the content.